IEEE Access
Multidisciplinary | Rapid Review | Open Access Journal

Received October 9, 2019, accepted November 6, 2019, date of publication November 11, 2019, date of current version November 21, 2019.

Digital Object Identifier 10.1109/ACCESS.2019.2953065

Improved Intra-Pulse Modulation Phase Calibration Algorithm With Accelerated Entropy Minimization Optimization

YUE LU[1], SHIYOU XU[2], YUE ZHANG[1], QI WU[1], AND ZENGPING CHEN[2]

[1]Science and Technology on Automatic Target Recognition Laboratory, National University of Defense Technology, Changsha 410073, China
[2]School of Electronics and Communication Engineering, Sun Yat-sen University, Guangzhou 510275, China

Corresponding author: Shiyou Xu (xushy36@mail.sysu.edu.cn)

This work was supported in part by the National Natural Science Foundation of China under Grant 6157010118.

ABSTRACT Intra-pulse modulation phase calibration is necessary in inverse synthetic aperture radar (ISAR) imaging of high-speed targets. Traditional intra-pulse phase error compensation strategies rarely handle the high-order and slow-time-variant phase components induced during the coherent processing interval. In this paper, a novel intra-pulse modulation phase calibration with a two-dimensional (2-D) parametric phase model is proposed. It models the intra-pulse phase errors as a 2-D time-variant polynomial with accommodation of both fast-time and slow-time modulation. Entropy minimization of high-resolution range profiles (HRRPs) is developed to retrieve the phase error parameters. Improved coordinate descent optimization solver is established by Levenberg-Marquardt (LM) algorithm in order to find the global optimum of entropy efficiently. Comparative experiments using both simulated and real measured data are performed to demonstrate the enhancements of the proposed algorithm.

INDEX TERMS Entropy minimization, intra-pulse modulation, inverse synthetic aperture radar (ISAR), phase error compensation.

I. INTRODUCTION

Inverse synthetic aperture radar (ISAR) is a well-established technology for generating high resolution image of non-corporative targets. Being capable of reconstructing detailed scattering structure of moving targets, ISAR has been widely used in both military and civilian fields [1]–[4]. One of the significant challenges ISAR imaging faces is the intra-pulse modulation error, such as amplitude error and phase error, in received signals. The intra-pulse modulation error can be caused by the following two reasons. Firstly, the nonlinearity of radar transmitting devices like mixer and multiplier, when used in wide-band situations, is inevitable [20]. This nonlinearity induces unexpected intra-pulse modulation. Although those errors usually are of low-frequency property, they would lead to strong smearing of the pulse response function. Because this error is relevant to the hardware, they are fast-time variant. Secondly, in real situations, the target's motion is often nonuniform with high velocity and acceleration. Prominent acceleration will induce a continuous phase modulation difference along the slow-time direction, yielding a slow-time-variant intra-pulse modulation in received signal. Intra-pulse modulation error introduced by the reasons above leads to defocused and blurred ISAR images, and due to the 2-D modulation characteristics, this problem is hard to deal with. What is more, intra-pulse modulation error calibration is the first step of ISAR imaging. Without a well calibration, the image will be seriously defocused, no matter how accurate the translational compensation is. As a result, the demand for methods of intra-pulse modulation error compensation is urgent.

Current calibration algorithms can be sorted into several categories. The first class is quadratic model-based calibration, such as map-drift algorithm (MDA) [4] and its modified versions [12]–[15]. MDA estimates the coefficient of quadratic phase error (QPE) according to the different functional forms of QPE across two half-length sub-apertures. A coherent MDA was proposed in [12], adopting traditional MDA into low contrast situations. They are more robust than general prominent-point-target-based algorithms, such as PGA [41]. However, MDA can only handle the QPE in fast-time direction, ignoring the higher orders and slow-time

The associate editor coordinating the review of this manuscript and approving it for publication was Hasan S. Mir.

variant term. Multiple map-drift algorithm (MAM) is the extension of MDA, which can estimate the higher-order phase error by dividing the full aperture into more than one sub-aperture [4]. Similar to MDA, MAM also ignores the slow-time variant feature of the phase error, and when the number of echoes is not enough, short-length sub-apertures will be used, degrading both the resolution and the signal-to-noise ratio. A phase distortion compensation method in the frequency domain based on the least squares estimation (LSE) is proposed in Liu Y, et al. [16]. This method models phase error as a second-order polynomial of frequency variable. The quadratic term is known via calibration tower, and the linear term induced by unknown transmitted delay time can be estimated through LSE. With this method, ISAR image quality can be improved. However, the method is based on the assumption that the phase error caused by the target motion has been compensated before, and the transmitted signal is received by direct intermediate frequency sampling (DIFS) technique. Therefore, it cannot handle the situation in which phase error is induced by the nonuniform motion of a target and the echo is received by dechirp process. The second class is the metric-based optimization method. These methods model the displacement as a polynomial of the time variable and construct the compensation function by estimating polynomial coefficients [7]. The estimation is often obtained through minimizing or maximizing a particular metric (entropy, contrast, and sharpness) [21]–[26]. Because of the use of global information, they are more robust and can obtain more accurate results compared with traditional methods. However, these methods are designed for fast-time variant phase error without any discussion on slow-time variant terms.

To solve the optimization, there are many standard methods available, such as the gradient descent algorithm, Newton's method, the simulated annealing algorithm, and the genetic algorithm. However, due to the influence of the inevitable noise, entropy functions of ISAR signal echo may not be smooth enough along with a lot of local minima. And entropy functions can be relatively flat which means the gradient is very small. Gradient-based algorithms, therefore, suffer a slow rate of convergence and can be trapped into local minima [27]. The standard Newton's method is also likely to stop in local minima, and it needs to compute the inverse of the Hessian matrix which brings lots of computation burdens, especially in multi-parameter situations [27]. Heuristic algorithms like simulated annealing algorithm and genetic algorithm always need considerable computation time and a complex parameter setting scheme [31]–[34].

Generally, the phase error caused by intra-pulse modulation is more crucial than the amplitude error. Herein we focus on the calibration of intra-pulse modulation phase error. Motivated by the 2-D time-variant characteristic of intra-pulse phase error, a novel intra-pulse modulation phase calibration for ISAR imaging is proposed in which parameters estimation is implemented in a fast and robust manner. We first model the phase error term as a high-order polynomial (cubic polynomial) with consideration of fast-time and slow-time modulation. Based on the model, we formulate the entropy minimum optimization of the high range resolution profiles (HRRPs). The entropy is used as the optimization metric to estimate the polynomial coefficients. Then, we propose a novel coordinate descent optimization scheme implemented by Levenberg-Marquardt (LM) method [27], [30]. It is revealed that the scheme will yield reliable convergence compared with standard Newton solver and direct parameter searching. By performing comparative experiments based on simulated and real measured data, the efficiency and robustness of the proposed algorithm can be proved. The main contributions of this work are listed as follows:

1) A novel intra-pulse phase error model is proposed with consideration of the fast-time and slow-time variant modulation error, induced by the nonlinearity of transmitting devices and high radial velocity and acceleration of the target. This model contains 2-D time-varying modulation information, which can produce an accurate error fitting.

2) An optimization scheme combining coordinate descent algorithm and Levenberg-Marquardt method is implemented to solve the optimum parameters, which can achieve global convergence and a fast convergent rate.

This paper is organized in the following manner. In section II, we establish the intra-pulse modulation model and analyze the impact of error parameters on imaging. General ISAR geometry and dechirped signal model are also recalled to maintain the integrity of the context. In section III, the algorithm for intra-pulse modulation phase calibration compensation based on coordinate descent method is presented in detail. Section IV demonstrates the experiment results of simulated and real measured data to verify the effectiveness of the proposed algorithm. Some conclusions are given in section V.

II. IMAGING GEOMETRY AND SIGNAL MODEL

This section firstly presents conventional ISAR imaging geometry and dechirped signal model [6]–[8]. And then, the characteristics of 2-D time-variant phase errors are also analyzed.

A. ISAR IMAGING GEOMETRY AND DECHIRPED SIGNAL MODEL

A three-dimensional ISAR geometry is illustrated in Fig. 1a. The cartesian coordinate system (χ_1, χ_2, χ_3) is the radar reference coordinate in which the object of interest is moving. The (χ_1', χ_2', χ_3') coordinate system is attached to the target and is often called the body coordinate of the target. r_0 denotes the distance between the radar and target, and the direction of r_0 is radar line-of-sight (LOS). It is well-known that ISAR geometry can be viewed as a two-dimensional model, as shown in Fig. 1b. In Fig. 1b, $R(t)$ denotes the instantaneous distance from the radar to the rotation center and $\Delta\theta$ represents the instantaneous rotational angel. They correspond to translation and rotation respectively [18].

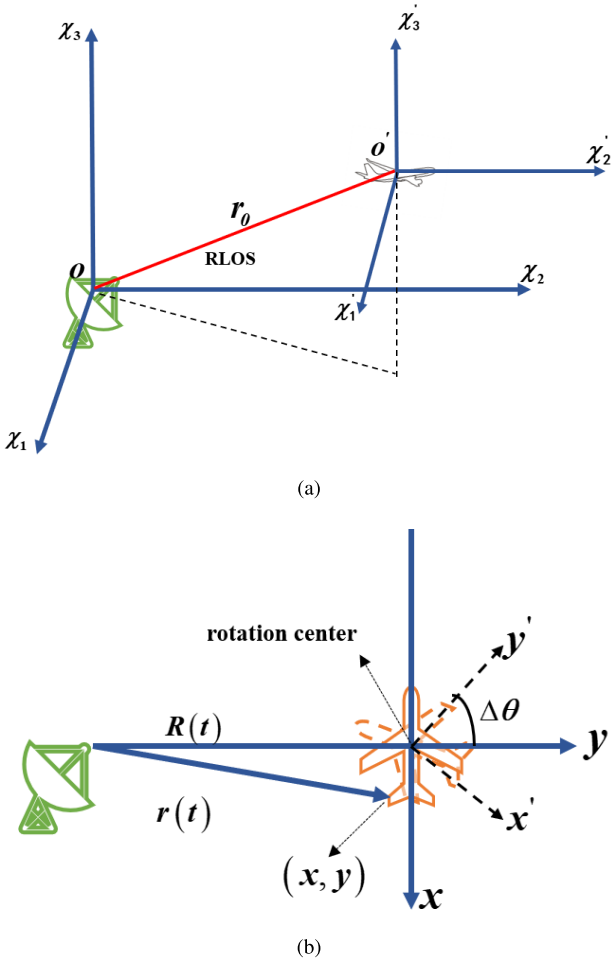

FIGURE 1. ISAR imaging geometry model. (a) Three-dimensional ISAR geometry; (b) 2-D rotational model.

In ISAR imaging, the linear-frequency-modulated (LFM) signal is often adopted in the imaging radar which is given by

$$s\left(\hat{t}\right) = rect\left(\frac{\hat{t}}{T_P}\right) \cdot \exp\left[j2\pi\left(f_c\hat{t} + \frac{1}{2}\gamma\hat{t}^2\right)\right] \tag{1}$$

where $rect\left(\tau\right) = \begin{cases} 1, |\tau| \le \frac{1}{2} \\ 0, |\tau| > \frac{1}{2} \end{cases}$, T_p is the pulse duration, f_c is the carrier frequency, γ is the chirp rate, and $\hat{t}$ is the fast time.

Suppose that there are K scatter points and the distance between the radar and scatter k is denoted as R_k, then the total echo of K scatter points can be written as

$$s_r\left(\hat{t}, t_m\right) = \sum_{k=1}^{K}\left\{\sigma_k rect\left(\frac{\hat{t} - t_k}{T_P}\right) \cdot \exp\left\{j2\pi\left[f_c\left(\hat{t} - t_k\right) + \frac{1}{2}\gamma\left(\hat{t} - t_k\right)^2\right]\right\}\right\} \tag{2}$$

where σ_k and c denotes the reflection intensity and velocity of light respectively, t_m is the slow time, and $t_k = 2 \cdot R_k/c$ is the time delay of scatter k's echo.

After the well-established dechirping technique [17], the signal echo becomes:

$$s_d\left(t_s\right) = \sum_{k=1}^{K}\left\{\sigma_k rect\left(\frac{t_s - \tau_{\Delta k}}{T_P}\right) \cdot \exp\left\{-j2\pi\left[\left(f_c + \gamma t_s\right)\tau_{\Delta k} - \frac{1}{2}\gamma\tau_{\Delta k}^2\right]\right\}\right\} \tag{3}$$

in (3), $t_s = \hat{t} - t_{ref}$, $t_{ref} = 2R_{ref}/c$ and $\tau_{\Delta k} = 2\left(R_k - R_{ref}\right)/c = t_k - t_{ref}$, where R_{ref} is the distance between the radar and the reference point, and t_{ref} means the time delay of the reference point's echo.

B. 2-D TIME-VARIANT PHASE ERROR MODEL

The causes of the intra-pulse modulation phase error have been analyzed in the section I. In this subsection, the proposed phase error model will be discussed, and the impact of the error parameters on ISAR imaging will also be given.

As we described in section I, the nonlinearity of radar transmitting devices can defocus the phase of effective signals, resulting in an extra intra-pulse modulation phase error, and this error is fast-time dependent. With consideration of the phase error term caused by this reason, the transmitted signal in (1) can now be expressed as

$$s\left(\hat{t}\right) = rect\left(\frac{\hat{t}}{T_P}\right) \cdot \exp\left[j2\pi\left(f_c\hat{t} + \frac{1}{2}\gamma\hat{t}^2\right)\right] \cdot \exp\left[j\Phi_{dev}\left(\hat{t}\right)\right] \tag{4}$$

where $\Phi_{dev}\left(\hat{t}\right)$ represents the phase error term induced by the transmitting device's nonlinearity.

According to the Taylor expansion, the error term above can be written as a high-order polynomial with respect to the fast-time term $\hat{t}$

$$\Phi_{dev}\left(\hat{t}\right) = d_0 + d_1\hat{t} + d_2\hat{t}^2 + d_3\hat{t}^3 + O\left(\hat{t}^4\right) \tag{5}$$

where $d_i, i = 1, 2, 3$ denotes polynomial coefficients, and $O\left(\hat{t}^4\right)$ is on behalf of error terms of fourth-order and above. The constant term on the right side of (5) has no influence on the range image; the linear term will only cause the shift of envelopes, which can be solved by range alignment. Therefore, they can be ignored in this phase error compensation stage. It also should be noted that, in this paper, we ignore $O\left(\hat{t}^4\right)$, namely, we define $\Phi_{dev}\left(\hat{t}\right)$ as a third-order polynomial.

With consideration of the extra phase term, the dechirped echo in (3) can be rewritten as

$$\begin{aligned} &s_d\left(t_s\right) \\ &= \sum_{k=1}^{K}\left\{\sigma_k rect\left(\frac{t_s - \tau_{\Delta k}}{T_P}\right) \cdot \exp\left\{-j2\pi\left[\left(f_c + \gamma t_s\right)\tau_{\Delta k} - \frac{1}{2}\gamma\tau_{\Delta k}^2\right]\right\}\Phi_{dev}\left(\hat{t} - t_k\right)\right\} \\ &= \sum_{k=1}^{K}\left\{\sigma_k rect\left(\frac{t_s - \tau_{\Delta k}}{T_P}\right)\right. \end{aligned}$$

$$\cdot \exp\left\{-j2\pi\left[\left(f_c+\gamma t_s\right)\tau_{\Delta k}-\frac{1}{2}\gamma\tau_{\Delta k}^2\right]\right\}\Phi_{dev}(t_s-\tau_{\Delta k})\Big\} \tag{6}$$

Therefore, the phase error caused by the transmitting device in dechirped echo is denoted by

$$\Phi_{dev}\left(t_s;\tau_{\Delta k}\right)=d_2(t_s-\tau_{\Delta k})^2+d_3(t_s-\tau_{\Delta k})^3 \tag{7}$$

In (7), for simplicity, we have discarded the constant and linear terms.

Fig. 2 illustrates the impact of the terms in (5) on the range profile. For simplicity, we use a scatter point located at $(10m, 10m)$ as the target, and the original point is used as the reference point. Dechirp technique is used to process the received signal which has 10GHz carrier frequency, 6GHz bandwidth, $0.3\mu s$ pulse duration, 6GHz sampling rate, and 100Hz PRF. From Fig. 2, it can be seen that the linear term shifts the range profile, but does not influence the degree of focus of the range profile; the quadratic term, however, badly defocuses the range profile, resulting in obviously broadening; the cubic term causes defocus as well, leading to asymmetric and distorted main lobe. With all the three kinds of terms above, the quality of the pulse compression is severely degraded.

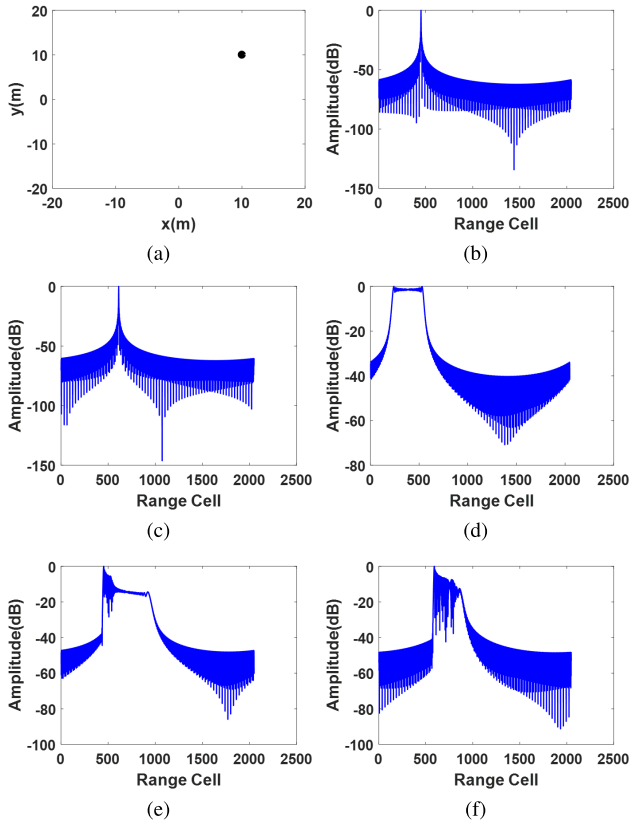

FIGURE 2. The impact of the nonlinearity of transmitting device. (a) The target model; (b) the range profile without error; (c) the range profile with the linear term only; (d) the range profile with the quadratic term only; (e) the range profile with the cubic term only; (f) the range profile with all the three terms.

The second reason for the intra-pulse modulation error is the high velocity and acceleration of the target. By referring [9], we give the following analysis.

According to (6), the phase of the first exponential term on the right-hand side can be rewritten as

$$\Phi\left(t_s,t_m\right)=-2\pi f_c\tau_{\Delta k}-2\pi\gamma t_s\tau_{\Delta k}+\pi\gamma\tau_{\Delta k}^2 \tag{8}$$

Assuming that the range of the scatter k to the radar at time $\left(\hat{t},t_m\right)$ is denoted by

$$R_k\left(\hat{t},t_m\right)=R_k\left(t_m\right)+v\left(t_m\right)\hat{t} \tag{9}$$

and the range of the reference point to the radar can be expressed as

$$R_{ref}\left(\hat{t},t_m\right)=R_{ref}\left(t_m\right)+v\left(t_m\right)t_{ref} \tag{10}$$

where $v\left(t_m\right)$ denotes the radial velocity of the target [9].

We model the radial velocity as a linear function of slow time

$$v\left(t_m\right)=at_m+v_0 \tag{11}$$

where a represents the acceleration. Equation (11) is consistent with most situations. According to (9) and (10), $\tau_{\Delta k}$ has the following form

$$\begin{aligned}\tau_{\Delta k}\left(t_m\right)&=2\left[R_k\left(\hat{t},t_m\right)-R_{ref}\left(\hat{t},t_m\right)\right]/c\\&=2\left[R_k\left(t_m\right)-R_{ref}\left(t_m\right)+v\left(t_m\right)\left(\hat{t}-t_{ref}\right)\right]/c\\&=2\left[\Delta R_{k0}+v\left(t_m\right)t_s\right]/c\end{aligned} \tag{12}$$

Take (12) into (8), the phase term can thus be written as

$$\begin{aligned}\Phi\left(t_s,t_m\right)=&-\frac{4\pi}{c}f_c\Delta R_{k0}-\frac{4\pi}{c}f_cv\left(t_m\right)t_s-\frac{4\pi}{c}\gamma t_s\Delta R_{k0}\\&-\frac{4\pi}{c}\gamma v\left(t_m\right)t_s^2+\frac{4\pi}{c^2}\gamma\Delta R_{k0}^2\\&+\frac{8\pi}{c^2}\gamma\Delta R_{k0}v\left(t_m\right)t_s+\frac{4\pi}{c^2}\gamma v^2\left(t_m\right)t_s^2\end{aligned} \tag{13}$$

In (13), the first and fifth terms are constant, they have no impact on the image quality. The second, third and sixth terms are linear, leading to the shift of the envelope, but they do not worsen the image quality and can be eliminated by translation compensation methods. The fourth and seventh terms are quadric, which will broaden the range spectrum and defocus the image [9].

Equation (13) can be rewritten with ignorance of the constant and linear terms as

$$\Phi_{mot}\left(t_s,t_m\right)=-\frac{4\pi}{c}\gamma\left(v\left(t_m\right)-\frac{v^2\left(t_m\right)}{c}\right)t_s^2 \tag{14}$$

where Φ_{mot} denotes that this phase term comes from the target's motion. With consideration of the fact that the velocity of the target is much less than that of the light, (14) can thus be approximated as

$$\Phi_{mot}\left(t_s,t_m\right)=-\frac{4\pi}{c}\gamma v\left(t_m\right)t_s^2 \tag{15}$$

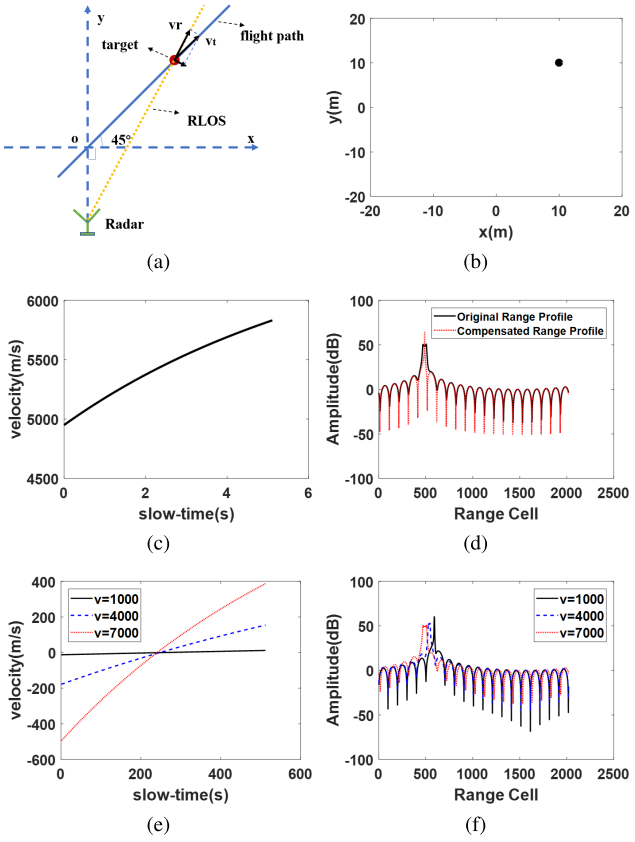

FIGURE 3. The impact of radial velocities. (a) The simulation situation; (b) the target model; (c) the radial velocity of 7000m/s along-track velocity; (d) the original and compensated range profiles; (e) different relative radial velocities of different along-track velocities; (f) comparison of range profiles of different velocities.

Take $v(t_m) = at_m + v_0$ into (15), and redefine the constant as coefficients of the polynomial, we can get

$$\Phi_{mot}(t_s, t_m) = (\beta_0 + \beta_1 t_m)\, t_s^2 = (\beta_0 + \beta_1 t_m)\left(\hat{t} - t_{ref}\right)^2 \quad (16)$$

where $\beta_0 = -4\pi\gamma v_0/c$, and $\beta_1 = -4\pi\gamma a t_m/c$.

Fig. 3 demonstrates the influence of $v(t_m)$ on the range profile. The target is the same as that in Fig. 2, i.e., a scatter point is located at $(10m, 10m)$, and the original point is chosen as the reference point for the dechirp receiving. The simulation situation is shown in Fig. 3a. The target starts at the origin and follows the flight path in the direction indicated by the arrow. vt in Fig. 3a denotes the velocity along the track, and vr is the radial velocity which will be analyzed. The distance from the radar to the origin is $100km$. The carrier frequency of the signal is 10GHz, the bandwidth is 6GHz, the sampling rate is 20MHz, the pulse duration is $100\mu s$, and PRF is 100Hz. First, we set $vt = 7000m/s$, i.e., the along-path velocity is constant. Under this circumstance, it can be seen in Fig. 3c that although the along-path velocity is constant, the radial velocity is varying with an acceleration of approximately $200m/s^2$. The solid line in Fig. 3d represents the range profile impacted by the high radial velocity and accelerations. Consistent with the previous analysis, the radial velocity results in spectrum broadening. After the radial velocity compensation by (15), the broadening effect can be eliminated, as the dashed line in Fig. 3d shows. Second, the along-path velocity is set as $1000m/s$, $4000m/s$, and $7000m/s$ respectively. We compare the effect of different radial velocity. The radial velocity changes in the three cases are shown in Fig. 3e, and, for comparison, they are all normalized by subtracting their mean values. Combining Figs. 3e-3f, we can conclude that larger radial velocity and accelerations cause wider main lobes, resulting in a highly defocused image. Consistent with former analysis, there are spectrum shifts for different radial velocities, which are caused by the linear term in (13).

We combine the two kinds of errors together with approximations that $t_s - \tau_{\Delta k} \approx \hat{t}$ and $\hat{t} - t_{ref} \approx \hat{t}$. The whole phase error is illustrated by

$$\Phi_\Delta\left(\hat{t}, t_m\right) = (\gamma_0 + \gamma_1 t_m) \cdot \hat{t}^2 + d\hat{t}^3 \quad (17)$$

where $\gamma_0 = \beta_0 + d_2$, $\gamma_1 = \beta_1$, and $d = d_3$.

Obviously, (17) is 2-D time variant, because it changes over fast and slow time.

The error-free part of the dechirped echo in a discrete form is defined as $s_0(m, n)$, where m is the index of slow time and n is the index of fast time. Likewise, the discrete form of the whole phase error is denoted by $\Phi_\Delta(m, n)$. Therefore, the echoed signal with phase error can be expressed as

$$\begin{aligned}\tilde{s}(m, n) &= s_0(m, n) \cdot \exp\{j\pi\Phi_\Delta(m, n)\} \\ &= s_0(m, n) \cdot \exp\left\{j\pi\left[(\gamma_0 + \gamma_1 m) \cdot n^2 + dn^3\right]\right\}\end{aligned} \quad (18)$$

Analyses of how the total phase error, i.e., a 2-D time-variant phase term, degrades the image quality will be given in the following paragraphs. We first demonstrate the spectrum of the phase error and then analyze its impact on range profile. It should be emphasized that we have normalized fast and slow time into $[-0.5, 0.5]$ according to the number of sampling points, hence, the values of parameters below are relative values.

Fig. 4 illustrates the spectrum of the phase error and the influence of the three parameters on the spectrum. The solid line in Figs. 4a-4c represents Fourier transform of $\Phi_\Delta(m, n)$ with respect to n, and the parameters are set as $\gamma_0 = 30$, $\gamma_1 = 50$, $d = -20$, and $m = 512$. It can be seen that the spectrum of the phase error is far from ideal Dirac function, and there exist obvious broadening and nonuniform amplitude. When this error term modulates the signal in the time domain, their spectrums are convolved in the frequency domain, which will cause broadening and distortion of range profile. The dashed line in Figs. 4a-4c shows the situations when $\gamma_0 = 0$, $\gamma_1 = 0$, and $d = 0$ respectively. It can be concluded that without γ_0 and γ_1, the broadening will be much smaller and the spectrum of the phase error is similar to Dirac function; if d is zero, the tilt of the main lobe will disappear. Fig. 4d demonstrates the slow-time variant characteristics of the phase error. We fix the values of parameters at $\gamma_0 = 30$, $\gamma_1 = 50$, and $d = -20$, and change m to 1, 256,

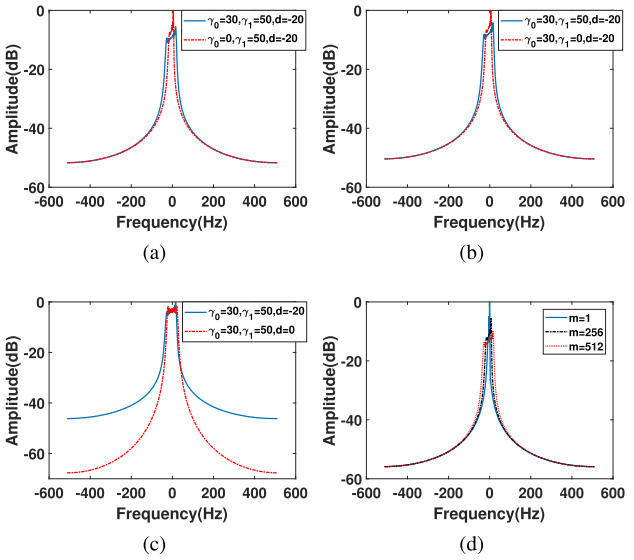

FIGURE 4. Simulation results of the phase error's spectrum. (a) The spectrum of the phase error with $\gamma_0 = 30$, $\gamma_1 = 50$, and $d = -20$, and the spectrum of the phase error with $\gamma_0 = 0$, $\gamma_1 = 50$, and $d = -20$; (b) the spectrum of the phase error with $\gamma_0 = 30$, $\gamma_1 = 50$, and $d = -20$, and the spectrum of the phase error with $\gamma_0 = 30$, $\gamma_1 = 0$, and $d = -20$; (c) the spectrum of the phase error with $\gamma_0 = 30$, $\gamma_1 = 50$, and $d = -20$, and the spectrum of the phase error with $\gamma_0 = 30$, $\gamma_1 = 50$, and $d = 0$; (d) the spectrum of the phase error with $m = 1$, $m = 256$, and $m = 512$ respectively.

and 512 respectively. It can be seen that with the increasing of m, i.e., the quadratic term, the spectrum gets wider.

Fig. 5 illustrates the influence of the three parameters on the one-dimensional range profile. We use the same target as that in Fig. 3. The radar transmits the LFM signal and receives echo using dechirp technique with a reference point $(x, y) = (0, 0)$. The carrier frequency is 10GHz and the bandwidth is 500MHz. The pulse width is $2\mu s$ and the PRF is 400Hz. Fig. 5b shows the ideal dechirped result with the elimination of RVP terms. The dashed line in Figs. 5c-5f is the dechirped result with phase error parameters $\gamma_0 = 30$, $\gamma_1 = 50$, and $d = -20$, $\gamma_0 = 0$, $\gamma_1 = 50$, and $d = -20$, $\gamma_0 = 30$, $\gamma_1 = 0$, and $d = -20$, and $\gamma_0 = 30$, $\gamma_1 = 50$, and $d = 0$ respectively. It can be seen that the existence of phase error leads to the broadening, tilt, and distortion of HRRP. By comparing Figs. 5d-5f, it can be concluded that γ_0 and γ_1 mainly cause the broadening of HRRP, and d results in the tilt of HRRP's main lobe. Fig. 5g is a scattering model of a plane and Fig. 5f is the imaging result with error parameters $\gamma_0 = 30$, $\gamma_1 = 50$, and $d = -20$. It can be seen that each scattering point is badly defocused, and the outline of the plane is blurred.

The scheme of phase error compensation is to first estimate the three parameters and then, construct compensation function to eliminate the phase error. Suppose the estimated value of γ_0, γ_1, and d is $\hat{\gamma}_0$, $\hat{\gamma}_1$, and $\hat{d}$, the compensation function can be written as

$$\tilde{\Phi}_{\Delta}(m, n) = \exp\left\{-j\pi\left[\left(\hat{\gamma}_0 + \hat{\gamma}_1 m\right) \cdot n^2 + \hat{d} n^3\right]\right\} \quad (19)$$

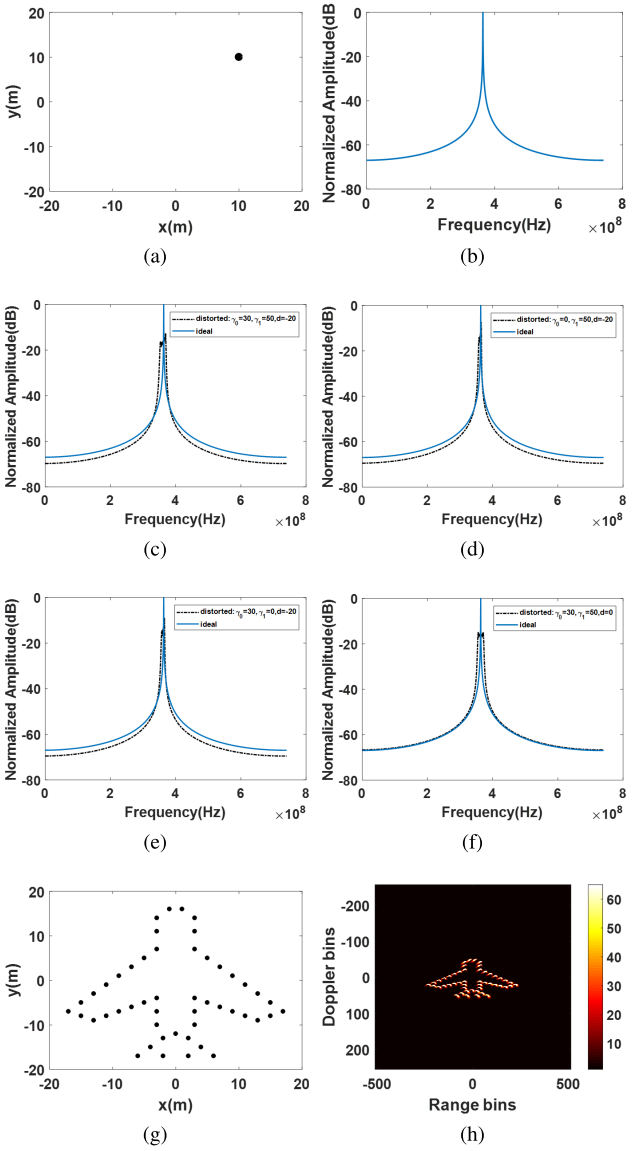

FIGURE 5. Simulation results of parameters' influence on the HRRP. (a) The model of a scattering point; (b) the HRRP of ideal dechirped signal; (c) the distorted HRRP with $\gamma_0 = 30$, $\gamma_1 = 50$, and $d = -20$, and the ideal HRRP; (d) the distorted HRRP with $\gamma_0 = 0$, $\gamma_1 = 50$, and $d = -20$, and the ideal HRRP; (e) the distorted HRRP with $\gamma_0 = 30$, $\gamma_1 = 0$, and $d = -20$, and the ideal HRRP; (f) the distorted HRRP with $\gamma_0 = 30$, $\gamma_1 = 50$, and $d = 0$, and the ideal HRRP; (g) a plane model; (h) the imaging result with the phase error.

Therefore, the phase error can be compensated by

$$s_c(m, n) = \exp\left\{-j\pi\left[\left(\hat{\gamma}_0 + \hat{\gamma}_1 m\right) \cdot n^2 + \hat{d} n^3\right]\right\} \cdot \tilde{s}(m, n) \quad (20)$$

In the next section, details of the algorithm to estimate parameters will be discussed.

III. PARAMETERS ESTIMATION BASED ON MINIMIZATION ENTROPY OPTIMIZATION

Section III will introduce the parameters estimation method based on the minimization entropy optimization. In order to increase the convergent rate and robustness of the

algorithm, we propose an optimization algorithm combining Levenberg-Marquardt method (LM method) and coordinate descent algorithm.

A. MINIMIZATION ENTROPY OPTIMIZATION

According to (20), the compensated signal can be achieved by multiplying polluted echoes by a compensation term $\exp\left\{-j\pi\left[(\gamma_0+\gamma_1 m)\cdot n^2+dn^3\right]\right\}$, and the HRRPs of M echoes after error compensation can be obtained by Fourier transform along range direction, i.e.,

$$\begin{aligned} g(m,n) &= \sum_{l=0}^{N-1} s_c(m,n;\gamma_0,\gamma_1,d)\cdot\exp\left(-j2\pi\frac{nl}{N}\right) \\ &= \sum_{l=0}^{N-1}\left\{\exp\left(-j\pi\gamma_0 n^2\right)\exp\left(-j\pi\gamma_1 mn^2\right)\right. \\ &\quad \left.\exp\left(-j\pi d n^3\right)\cdot\tilde{s}(m,n)\cdot\exp\left(-j2\pi\frac{nl}{N}\right)\right\} \end{aligned} \tag{21}$$

In order to measure the degree of focus of HRRPs, the entropy function is introduced. Entropy is one of the most suitable functions to represent the sharpness of an image, and it is a widely used principle in ISAR imaging [21]–[24]. It is based on the assumption that if the signal is error-free, the shape of its HRRP will be sharpest which means the energy of HRRP is well-focused.

From (21), it can be seen that HRRP is the function of γ_0, γ_1, and d, therefore the entropy of HRRPs is also the function of γ_0, γ_1, and d, which can be written as

$$\begin{aligned} E(\gamma_0,\gamma_1,d) = -\frac{1}{S_g}\sum_{h=0}^{M-1}\sum_{l=0}^{N-1}\left\{|g(\gamma_0,\gamma_1,d)|^2\right. \\ \left.\cdot\ln|g(\gamma_0,\gamma_1,d)|^2\right\}+\ln S_g \end{aligned} \tag{22}$$

where S_g is the intensity of HRRPs, and it can be expressed as

$$S_g = \sum_{h=0}^{M-1}\sum_{l=0}^{N-1}|g(\gamma_0,\gamma_1,d)|^2 \tag{23}$$

The problem of estimating parameters γ_0, γ_1, and d can be abstracted as the following form according to minimization entropy principle:

$$\left\langle\hat{\gamma}_0,\hat{\gamma}_1,\hat{d}\right\rangle = \arg\min_{\gamma_0,\gamma_1,d} E(\gamma_0,\gamma_1,d) \tag{24}$$

So far, the model of optimization has been established. It is an optimization problem for a three-parameter search. Fig. 6 illustrates the variation of the entropy function of a simple model. Fig. 6a shows the target's model and (b) denotes the HRRPs distorted with phase error and noise. Figs. 6c–6e represent the independent variation of entropy with respect to γ_0, γ_1, and d respectively. It can be seen that the optimization process will face the challenges of local minima and relatively flat cost function. The next subsection will introduce the workflow of the proposed algorithm to solve the problem described in (24).

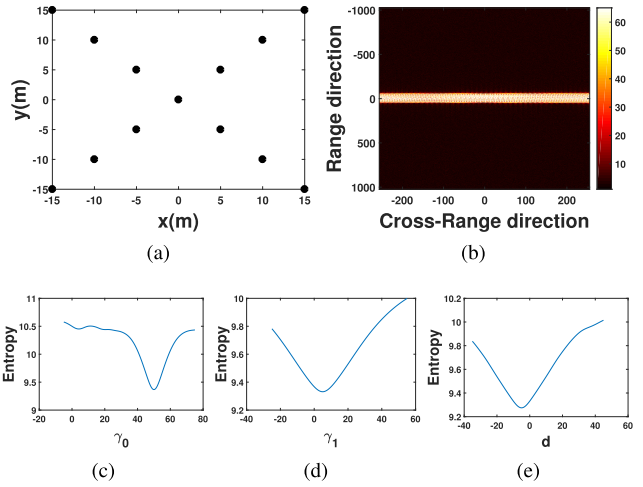

FIGURE 6. Simulation results of a simple model's entropy function. (a) The model of the target; (b) the distorted HRRPs; (c) the variation of entropy with respect to γ_0; (d) the variation of entropy with respect to γ_1; (e) the variation of entropy with respect to d.

B. WORKFLOW OF THE PROPOSED ALGORITHM

In this paper, a coordinate descent algorithm [35], [39], [40] combined with the LM method is proposed. It can be proved that this scheme has better robustness and a faster rate of convergence. The result can be seen in the next section.

The idea of coordinate descent algorithm is that by minimizing a multivariable function $F(\boldsymbol{\theta})$ along a certain direction at one time, i.e., solving a series of univariate optimization in a loop (epoch), the optimal point $\boldsymbol{\theta}_{opt}$ can be found. Coordinate descent algorithm is an iterative method in which each iteration is obtained by approximately minimizing the cost function with respect to a single parameter while fixing the remaining parameters at their values from the current iteration [35].

Assume that vector $\boldsymbol{\theta} = [\gamma_0, \gamma_1, d]^T$ denotes the parameters vector, θ_k is the kth parameters in $\boldsymbol{\theta}$, and $\boldsymbol{\theta}^{(i,k)}$ represents the vector of three phase error parameters at the ith iteration in which the first $k-1$ parameters' value has been updated. For example, $\boldsymbol{\theta}^{(i,3)} = \left[\gamma_0^{(i+1)}, \gamma_1^{(i+1)}, d^{(i)}\right]$ means in the ith iteration, γ_0 and γ_1 have been updated, and d needs to be searched. Therefore, the problem now is a one-dimensional search with respect to θ_k. Assume that the updating value of $\theta_k^{(i)}$ is $\Delta\theta_k$, we can correct HRRPs after obtaining $\theta_k^{(i+1)}$ as follows

$$\begin{aligned} E\left(\theta^{(i,k)};\Delta\theta_k\right) = -\frac{1}{S_g}\sum_{h=0}^{M-1}\sum_{l=0}^{N-1}\left\{\left|g\left(\theta^{(i,k)};\Delta\theta_k\right)\right|^2\right. \\ \left.\cdot\ln\left|g\left(\theta^{(i,k)};\Delta\theta_k\right)\right|^2\right\}+\ln S_g \end{aligned} \tag{25}$$

where image intensity is

$$S_g = \sum_{h=0}^{M-1}\sum_{l=0}^{N-1}\left|g\left(\boldsymbol{\theta}^{(i,k)};\Delta\theta_k\right)\right|^2 \tag{26}$$

To solve one-dimensional optimization in each iteration, we use LM method. By referring [30], we will briefly introduce LM method and its comparison with gradient descent method and Newton's method.

Traditional line search methods are gradient descent and Newton's method. The one-dimensional gradient descent updates the pth parameter based on the following rule

$$\theta_k^{(p+1)} = \theta_k^{(p)} - \mu \frac{\partial E^{(p)}\left(\theta_k^{(p)}\right)}{\partial \theta_k^{(p)}} \tag{27}$$

where μ is the step length factor and $\partial E^{(p)}\left(\theta_k^{(p)}\right)/\partial\theta_k^{(p)}$ is the first-order derivative (gradient) of the cost function at $\theta_k^{(p)}$. Note that the superscript i in (25)–(26) represents the ith outer loop (epoch) of the coordinate descent method and p in (27) denotes the pth iteration of the one parameter searching in coordinate descent method. Gradient descent is suitable for very simple models, but its convergence can take a long time for complex models. For example, when the cost function is very steep, a small step should be used to avoid crossing the optimal point, and on the contrary, when the error surface is flat, a large step is wanted otherwise time consumption is considerable. However, gradient descent only uses gradient information which results in the situation that in the steep region, step length is large and in the shallow region, step length is small. This characteristic degrades performance [30].

The pth update of Newton's method is given by

$$\theta_k^{(p+1)} = \theta_k^{(p)} - \mu\left(\frac{\partial^2 E^{(p)}\left(\theta_k^{(p)}\right)}{\partial\left(\theta_k^{(p)}\right)^2}\right)^{-1} \frac{\partial E^{(p)}\left(\theta_k^{(p)}\right)}{\partial \theta_k^{(p)}} \tag{28}$$

where $\partial^2 E^{(p)}\left(\theta_k^{(p)}\right)/\partial\left(\theta_k^{(p)}\right)^2$ represents second-order derivative (a special case of Hessian matrix) of the cost function at $\theta_k^{(p)}$. Compared with gradient-based methods, Newton's method makes use of curvature information which speeds convergence up enormously. However, when the error surface is not smooth enough, the second-order derivative can be negative which will not guarantee that the update direction is descent direction. What is more, in Newton's method, the quadratic approximation of the cost function is used, which denotes that the accurate result can be obtained only in the locations near the optimal point.

LM method blends the two extremes above [30]. The update rule is

$$\theta_k^{(p+1)} = \theta_k^{(p)} - \left(\frac{\partial^2 E^{(p)}}{\partial\left(\theta_k^{(p)}\right)^2} + \mu \cdot \frac{\partial^2 E^{(p)}}{\partial\left(\theta_k^{(p)}\right)^2}\right)^{-1} \frac{\partial E^{(p)}}{\partial \theta_k^{(p)}} \tag{29}$$

If the value of μ is large, (29) is approximate to (27) which is a quasi-gradient descent method and algorithm can still get benefit from curvature information. On the other hand, if μ is small, (29) approaches (28), i.e., the Newton's method. The insight of this method is that by adjusting μ, we can use gradient-based method until the minimum is approached, then switch to Newton's method in order to get high performance [30]. The distance to the minimum can be estimated by the change of the error value.

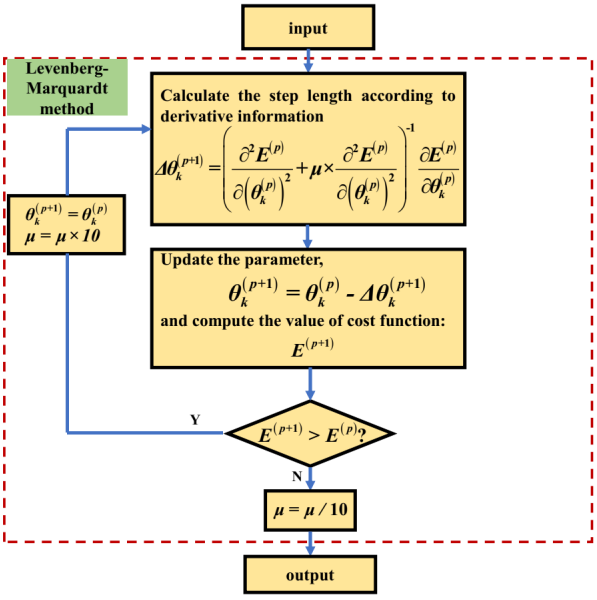

FIGURE 7. Flowchart of Levenberg-Marquardt method.

The LM method adjusts the blending factor μ according to the scheme below [30].

1) Update parameters using (29) directly.

2) Compute the value of cost function using updated parameters.

3) If the cost function increases because of the update in step 1, then reset parameters to their previous value and multiply μ by a factor of 10. Return to step 1 and repeat.

4) If cost function decreases after the update, then accept the new value of parameters and divide μ by a factor of 10.

Fig. 7 shows the block diagram of the LM method.

From (29), it can be seen that the first-order and second-order derivative of entropy function with respect to θ_k, i.e., γ_0, γ_1, and d are needed.

The formulas of HRRP and its entropy function has been given in (21), (22), and (23). The partial derivative of $E(\boldsymbol{\theta})$ with respect to the kth parameter θ_k can be expressed as

$$\frac{\partial E(\boldsymbol{\theta})}{\partial \theta_k} = -\frac{1}{S_g} \sum_{h=0}^{M-1} \sum_{l=0}^{N-1} (1 + \ln|g(\boldsymbol{\theta})|^2) \frac{\partial |g(\boldsymbol{\theta})|^2}{\partial \theta_k} \tag{30}$$

Since

$$\frac{\partial |g(\boldsymbol{\theta})|^2}{\partial \theta_k} = 2Re\left\{g^* \frac{\partial g}{\partial \theta_k}\right\} \tag{31}$$

Therefore, in order to get (31), we must first obtain $\partial g/\partial\theta_k$.

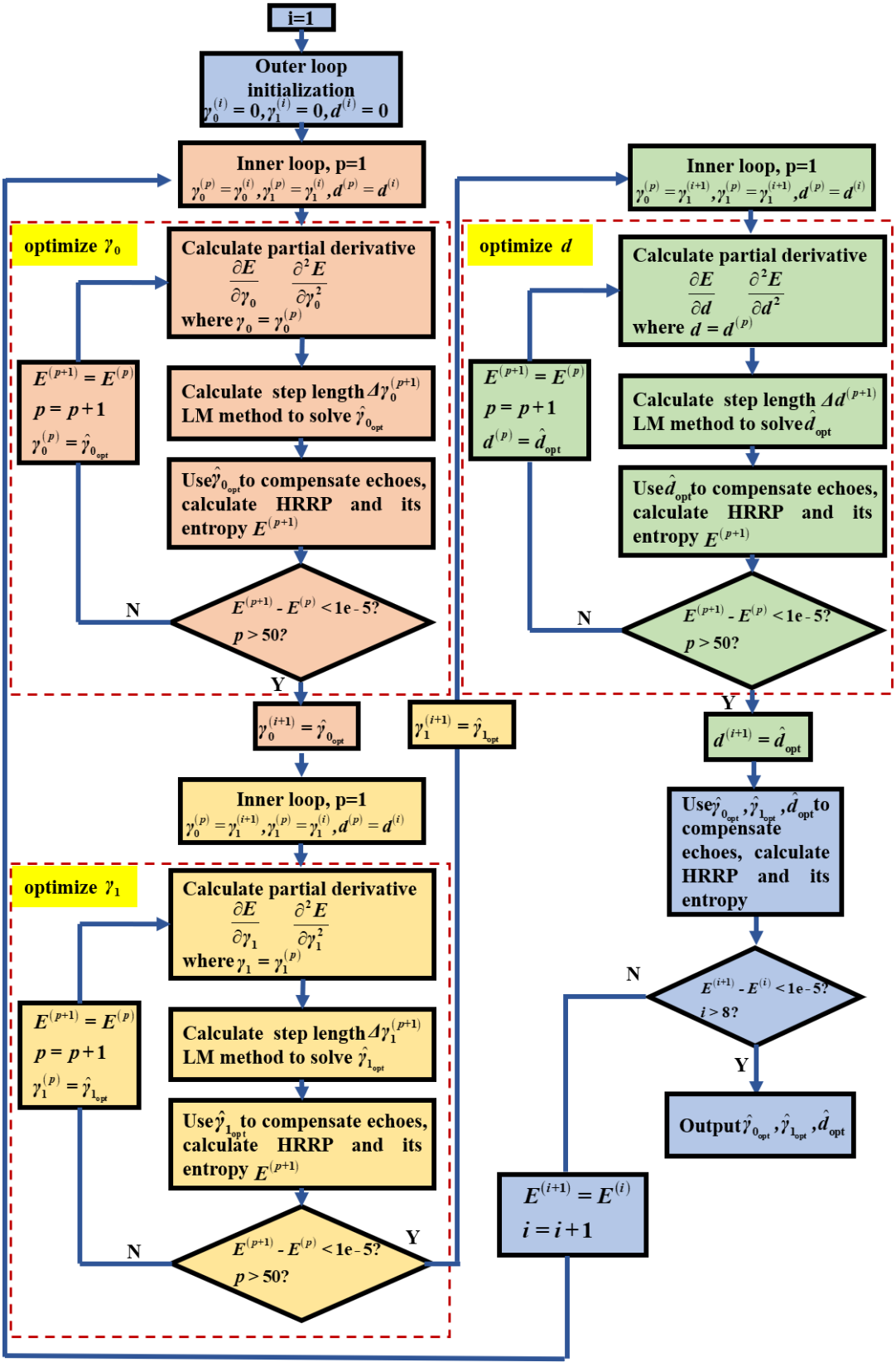

FIGURE 8. Block diagram of the proposed algorithm.

From (21), we can obtain the partial derivative of $g(\boldsymbol{\theta})$ with respect to θ_k, i.e., γ_0, γ_1, and d which are expressed as

$$\frac{\partial g(\boldsymbol{\theta})}{\partial \gamma_0} = \sum_{l=0}^{N-1} \left\{ \left(-j\pi n^2\right) \exp\left(-j\pi\gamma_0 n^2\right) \exp\left(-j\pi\gamma_1 mn^2\right) \exp\left(-j\pi d n^3\right) \tilde{s}(m,n) \exp\left(-j2\pi \frac{nl}{N}\right) \right\} \tag{32}$$

$$\frac{\partial g(\boldsymbol{\theta})}{\partial \gamma_1} = \sum_{l=0}^{N-1} \left\{ \left(-j\pi mn^2\right) \exp\left(-j\pi\gamma_0 n^2\right) \exp\left(-j\pi\gamma_1 mn^2\right) \exp\left(-j\pi d n^3\right) \tilde{s}(m,n) \exp\left(-j2\pi \frac{nl}{N}\right) \right\} \tag{33}$$

$$\frac{\partial g(\boldsymbol{\theta})}{\partial d} = \sum_{l=0}^{N-1} \left\{ \left(-j\pi n^3\right) \exp\left(-j\pi\gamma_0 n^2\right) \exp\left(-j\pi\gamma_1 mn^2\right) \exp\left(-j\pi d n^3\right) \tilde{s}(m,n) \exp\left(-j2\pi \frac{nl}{N}\right) \right\} \tag{34}$$

Take (32)–(34) into (30) and (31), partial derivative of $E(\boldsymbol{\theta})$ with respect to γ_0, γ_1, and d can be solved.

The second-order partial derivative of $E(\boldsymbol{\theta})$ with respect to kth parameters θ_k can be written as

$$\frac{\partial^2 E(\boldsymbol{\theta})}{\partial \theta_k^2} = -\frac{1}{S_g} \sum_{h=0}^{M-1} \sum_{l=0}^{N-1} \left(1 + \ln|g(\boldsymbol{\theta})|^2\right) \frac{\partial^2 |g(\boldsymbol{\theta})|^2}{\partial \theta_k^2} - \frac{1}{S_g} \sum_{h=0}^{M-1} \sum_{l=0}^{N-1} \frac{1}{|g(\boldsymbol{\theta})|^2} \left(\frac{\partial |g(\boldsymbol{\theta})|^2}{\partial \theta_k}\right)^2 \tag{35}$$

Since

$$\frac{\partial^2 |g(\boldsymbol{\theta})|^2}{\partial \theta_k^2} = 2Re\left[\left(\frac{\partial g(\boldsymbol{\theta})}{\partial \theta_k}\right)^* \left(\frac{\partial g(\boldsymbol{\theta})}{\partial \theta_k}\right) + g(\boldsymbol{\theta})^* \frac{\partial^2 g(\boldsymbol{\theta})}{\partial \theta_k^2} \right] \tag{36}$$

The first-order partial derivative of $g(\boldsymbol{\theta})$ with respect to $\boldsymbol{\theta_k}$, i.e., γ_0, γ_1, and d has been given in (32)–(34), therefore, in order to get (35), we must first obtain $\partial^2 g(\theta)/\partial\theta_k^2$

From (32)–(34), the second-order partial derivative of $g(\boldsymbol{\theta})$ with respect to θ_k can be derived:

$$\frac{\partial^2 g(\boldsymbol{\theta})}{\partial {\gamma_0}^2} = \sum_{l=0}^{N-1} \left\{ \left(-\pi^2 n^4\right) \exp\left(-j\pi\gamma_0 n^2\right) \exp\left(-j\pi\gamma_1 mn^2\right) \exp\left(-j\pi d n^3\right) \tilde{s}(m,n) \exp\left(-j2\pi \frac{nl}{N}\right) \right\} \tag{37}$$

$$\frac{\partial^2 g(\boldsymbol{\theta})}{\partial {\gamma_1}^2} = \sum_{l=0}^{N-1} \left\{ \left(-\pi^2 m^2 n^4\right) \exp\left(-j\pi\gamma_0 n^2\right) \exp\left(-j\pi\gamma_1 mn^2\right) \exp\left(-j\pi d n^3\right) \tilde{s}(m,n) \exp\left(-j2\pi \frac{nl}{N}\right) \right\} \tag{38}$$

$$\frac{\partial^2 g(\boldsymbol{\theta})}{\partial d^2} = \sum_{l=0}^{N-1} \left\{ \left(-\pi^2 n^6\right) \exp\left(-j\pi\gamma_0 n^2\right) \exp\left(-j\pi\gamma_1 mn^2\right) \exp\left(-j\pi d n^3\right) \tilde{s}(m,n) \exp\left(-j2\pi \frac{nl}{N}\right) \right\} \tag{39}$$

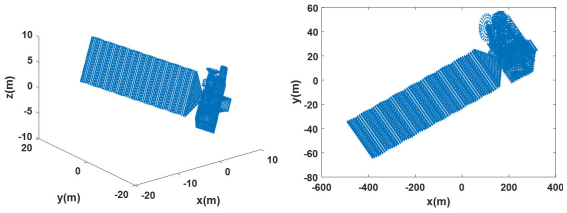

(a) (b)

FIGURE 9. Scattering model of a simulated satellite; (a) the 3-D model; (b) the 2-D projection model.

Take (37)–(39) into (35) and (36), the second order partial derivative of $E(\boldsymbol{\theta})$ with respect to γ_0, γ_1, and d can be solved. Derivation of (31) and (36) can be seen in the appendix.

Fig. 8 displays the workflow of the whole algorithm. In Fig. 8, the initial value of γ_0, γ_1, and d is set zero. Thanks to the robustness of the proposed algorithm, it is suitable to start at zero for most real situations. There are outer and inner loops in the workflow. The inner loop is for the one-dimensional parameter searching for γ_0, γ_1, and d respectively; after one outer loop (epoch), three parameters' values are updated. The stop condition for outer and inner loops is both based on the principle that if the cost function's value does not change obviously (less than 1e-5) or loop times has exceeded the set maximum loop times, the algorithm will has little effect on optimization, therefore, the iteration can be stopped. The blending factor μ of the LM method is set to 1e-3 which is an empirical value.

In the next section, both simulated and real-measured datasets are used to confirm the effectiveness and robustness of the proposed algorithm.

IV. EXPERIMENTS AND PERFORMANCE ANALYSIS

In this section, both simulated and real measured data are used to validate the effectiveness and robustness of the proposed algorithm. Two sets of experiments are performed with ISAR signal echo data. In the experiments using simulated data, artificial phase error and noise are introduced to validate the correctness of the proposed algorithm; Real measured Yak-42 data are used to further analyze the performance of the algorithm. Entropy and contrast are used to evaluate the image quality to show the improvement of error compensation. Algorithms of direct parameter searching and standard Newton's method are also used as comparisons. It must be noted that the standard Newton's method here mainly refers to searching three parameters at the same time, and in order to get the best comparison result, we use Broyden-Fletcher-Goldfarb-Shanno (BFGS) approximation to implement Newton's method. The computation platform is based on Windows 10 64-bit operating system, Intel Core i5-9300H@2.40GHz CPU, 8GB memory and MATLAB Version 2017b. All the experimental results show the advantages of the proposed method.

A. KA-BAND SIMULATION EXPERIMENT

This subsection demonstrates the simulation experiment results. A scattering model of a satellite is shown in Fig. 9.

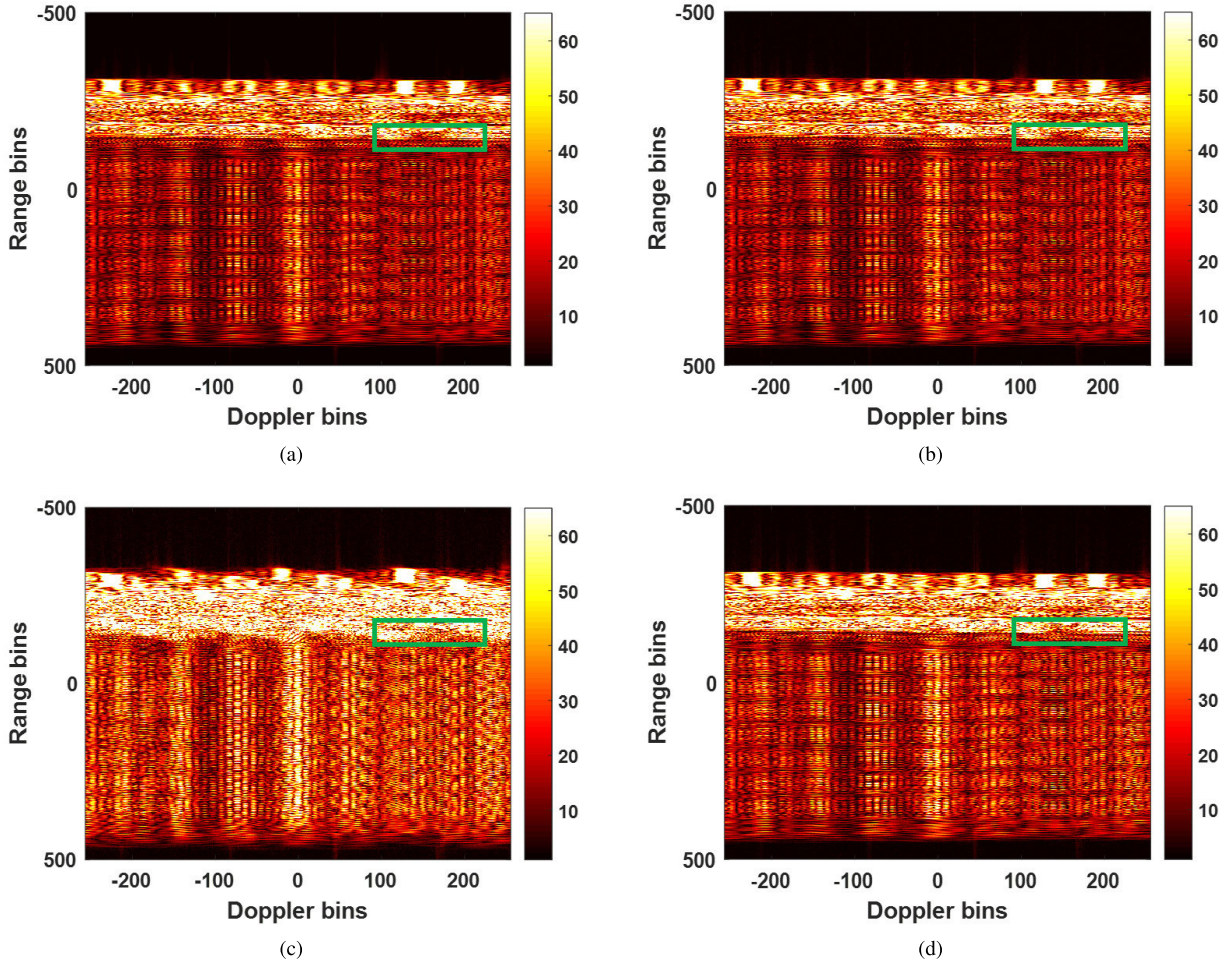

FIGURE 10. Simulation results of HRRPs. (a) The ideal HRRPs; (b) the HRRPs with noise; (c) the HRRPs with noise and phase error; (d) the compensated result of HRRPs.

TABLE 1. Parameters of simulated radar system.

Bandwidth	4GHz
Pulse Width	0.256μs
PRF	100Hz
Sampling Rate	4GHz
Carrier Frequency	30GHz

The main parameters of the simulated Ka-band radar system are demonstrated in Table 1. The size of echo data is 4096 $\times$ 512 (range$\times$azimuth). Phase error parameters are γ_0= 50, γ_1= 15, and d = 5. Complex Gaussian white noise is added with 20dB SNR. The purpose of this experiment is to illustrate the effectiveness of the proposed algorithm. The raw echo is generated by frequency domain correlation echo generation method [36], [37].

Fig. 10 illustrates the influence of the phase error and noise on the HRRPs and also demonstrates the effect of compensation through the proposed algorithm. Fig. 10a is the HRRPs of the ideal case, i.e., without phase error and noise. Fig. 10b is the HRRPs only polluted by noise. Compared with Figs. 10a–10b, it can be seen that the existence of noise increases the intensity of the background. The proposed method does not contain the noise-suppression effect, so Fig. 10b can be viewed as the upper bound of performance. Fig. 10c is the HRRPs contaminated by noise and the phase error with given parameters. From Figs. 10b–10c, the broadening effect of the phase error in range direction can be seen obviously. Compare the highlighted regions in Fig. 10, we can see that the ''trough'' of HRRPs disappears in Fig. 10c as a result of the phase error, which means the image is blurred and detailed information is lost. The compensated HRRPs obtained by the proposed method is shown in Fig. 10d, and it can be seen that Fig. 10d has very little difference with Fig. 10b. The ''trough'' is recovered in the highlighted region and the edge of HRRPs is very sharp compared with Fig. 10c. The entropy of Fig. 10c is 11.8311, and that of Fig. 10d is 11.7651. From the perspective of HRRPs, the proposed method is effective.

In Fig. 11, we display imaging results in different situations, and Table 2 demonstrates the parameters estimation result. All the results show the superiority of the proposed algorithm. Fig. 11a is the imaging result of error-free and

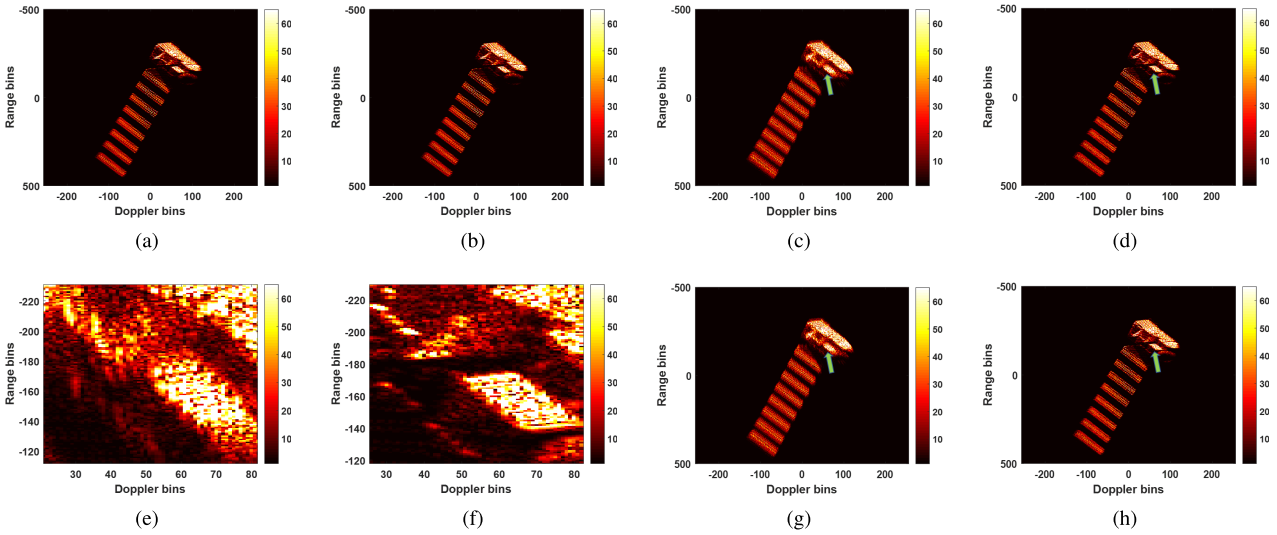

FIGURE 11. Simulation results of ISAR images. (a) The image of ideal case; (b) the imaging result with noise only; (c) the imaging result with the phase error and noise; (d) the imaging result obtained by the proposed method; (e) the zoom-in version of the arrow-point regions in (c); (f) the zoom-in version of the arrow-point regions in (d); (g) the imaging result with standard Newton's method; (h) the imaging result with direct parameter searching.

TABLE 2. Actual and estimated phase error parameters.

	γ_0	γ_1	d
actual value	50	15	5
estimated value	50.6164	14.4155	5.0726

TABLE 3. Comparison of image quality of polluted and compensated results.

	polluted by noise	polluted by noise and phase error	compensated result
contrast	3.9101	3.3414	3.8866
entropy	9.4190	9.7693	9.4332

noise-free signal echoes. Fig. 11b is the imaging result of the signal echoes with noise only. For the same reason of Fig. 10b, Fig. 11b is the upper bound of imaging performance. Fig. 11c is the image polluted by phase error and noise, and it can be seen that the image is badly defocused with blurred edges and unrecognizable parts (especially those pointed by arrows). The enhanced quality is obtained through compensating by the proposed method, and the result is displayed in Fig. 11d. Comparing the regions pointed by arrows (their zoom-in version can be seen in Fig. 11e and Fig. 11f respectively), we can see that detailed information of the target model is recovered by the algorithm, and small components of the target can be distinguished. The sharpness of the edges in Fig. 11d is similar to that in Figs. 11a–11b. Table 3 shows the evaluation of image quality based on entropy and contrast principles. Images in Figs. 11b–11d are all evaluated as a comparison. Through the value of contrast and entropy, it can be concluded that the quality of the compensated result is close to that of the image with noise only. Therefore, the correctness of the proposed method is validated.

To verify the robustness of the algorithm, experiments under different SNRs (from 10dB to −10dB) are also performed. Fig. 12 shows the results. The ideal ISAR images of the target under different SNRs are in the first column. The contaminated images with phase error parameters $\gamma_0 = 50$, $\gamma_1 = 15$, and $d = 5$ are demonstrated in the second column, and the compensated results of the proposed method are in the third column. HRRPs' entropy curves against iteration number are in the right column. We can see that even in the -10dB SNR, well-focused image can be obtained, and the entropy curves are always convergent under different SNRs. Compare the entropy and contrast of ideal, contaminated, and compensated images, we can conclude that through the proposed method, imaging quality is enhanced. What is more, 200 times Monte Carlo experiments under different SNRs are executed to further evaluate the robustness of the algorithm. The mean square error of phase parameters between theoretical and estimated values can be defined as

$$\begin{cases} MSE_{\gamma_0} = \sum_{n=1}^{N} \left[\hat{\gamma}_0(n) - \gamma_{0ideal}\right]^2 / N \\ MSE_{\gamma_1} = \sum_{n=1}^{N} \left[\hat{\gamma}_1(n) - \gamma_{1ideal}\right]^2 / N \\ MSE_{d} = \sum_{n=1}^{N} \left[\hat{d}(n) - d_{ideal}\right]^2 / N \end{cases} \tag{40}$$

where N denotes the Monte Carlo times, $\left(\hat{\gamma}_0, \hat{\gamma}_1, \hat{d}\right)$ and $(\gamma_{0ideal}, \gamma_{1ideal}, d_{ideal})$ represent estimated and theoretical values respectively. Fig. 13 illustrates the MSE curve against different SNRs. We can see that the estimated result can be of high accuracy when SNR is above -5dB. The reason why the MSE is relatively high when SNR is below -5dB is that

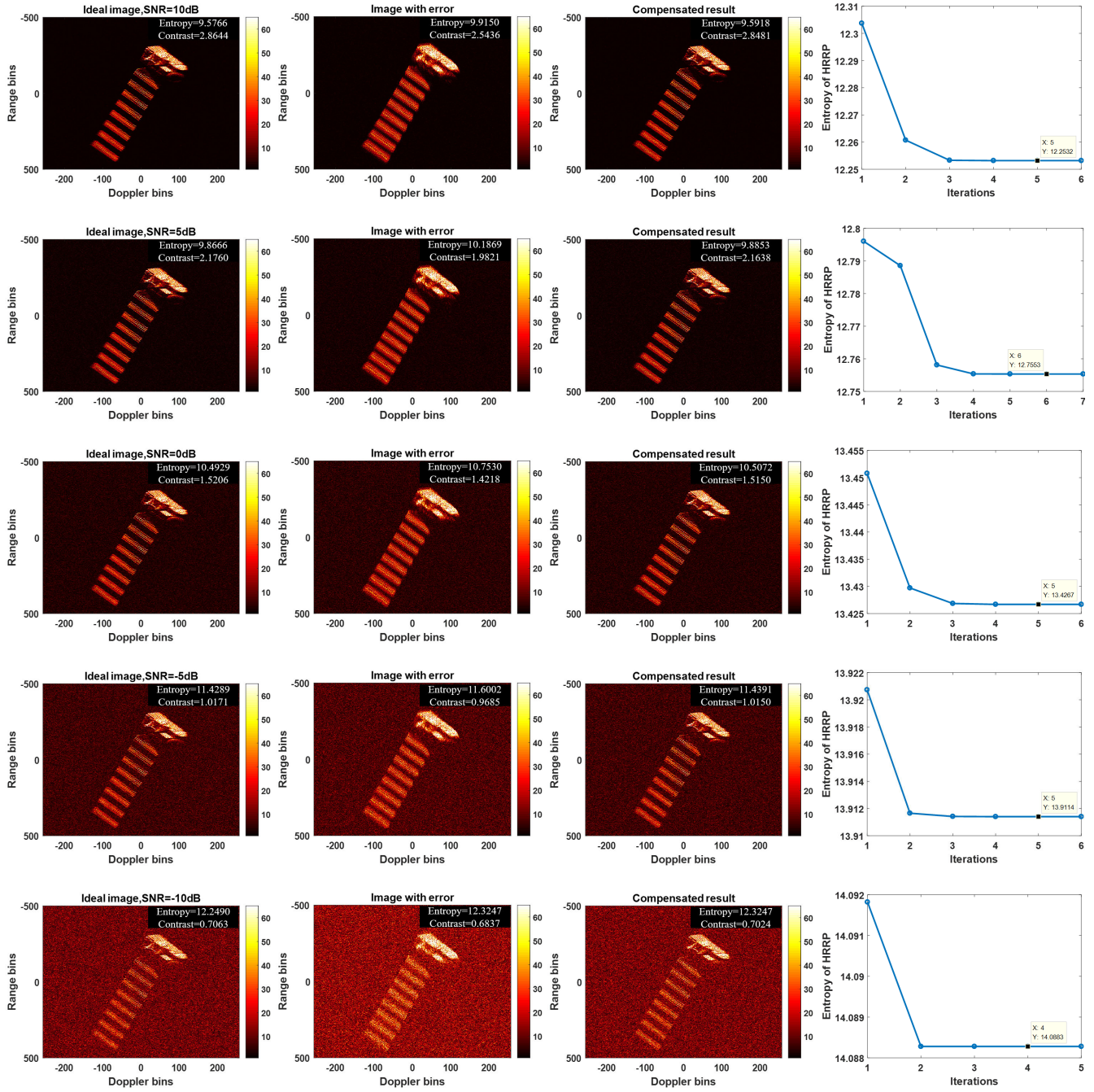

FIGURE 12. Simulation results under different SNRs.

the RCS of the solar panel of the simulated satellite is low, as a result, the scatter points on the solar panel cannot be distinguished in range profile when SNR is below -5dB. Fig. 14 shows this phenomenon. Through noise test and Monte Carlo experiment above, the robustness of the proposed method can be verified.

The algorithm of standard Newton's method and direct parameter searching is also used as a comparison to further verify the robustness and efficiency of the proposed algorithm.

We first use standard Newton's method. The difference between standard Newton's method and the proposed algorithm is that standard Newton's method searches three parameters simultaneously and has a more complex computation scheme. Fig. 11g demonstrates the compensated result of Newton's method. It can be seen that the effect of compensation is not very well. Blurred parts still exist in the image and detailed information is not fully recovered. The highlighted regions clearly show the defocus of the image. The reason for the poor performance of standard Newton's method is

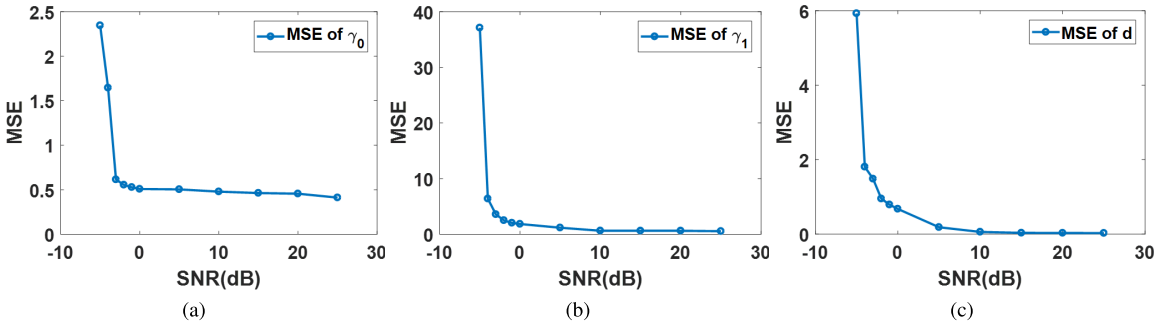

FIGURE 13. MSE curves of three parameters. (a) MSE of γ_0; (b) MSE of γ_1; (c) MSE of d.

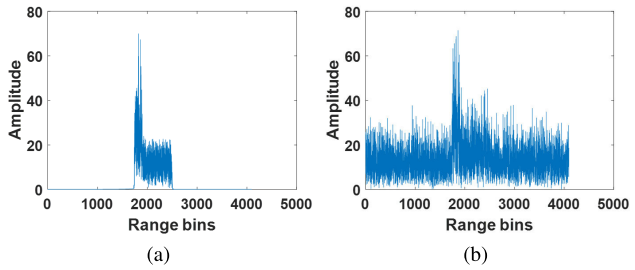

FIGURE 14. Range profiles comparison. (a) The ideal range profile; (b) the range profile under -5dB SNR.

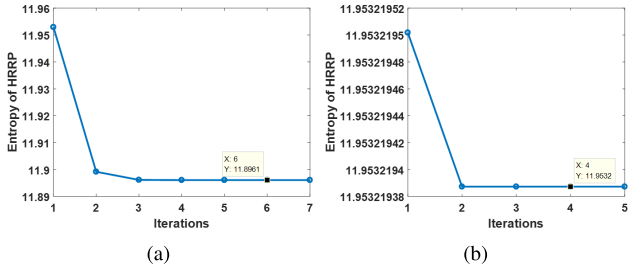

FIGURE 15. Convergence curves of the cost function. (a) The cost function's convergence curve of the proposed algorithm; (b) the cost function's convergence curve of standard Newton's method.

that it searches three parameters simultaneously which will encounter high risk to stop at local minima. In Fig. 15, the convergence curves of the two algorithms are illustrated, and the error margin is both 1e-5. It can be seen that the convergence value of the proposed algorithm is smaller than that of standard Newton's method. The robustness of standard Newton's method is not as good as that of the proposed method. The convergence time of these two methods is demonstrated in Table 4, and the working platform has been illustrated at the very beginning of this section. The run time of the proposed algorithm is longer than that of the standard Newton's method because the standard Newton's method stops earlier for some local minima. Note that Fig. 15a is the entropy variation against outer iterations of the proposed method, therefore the runtime per iteration is longer.

We then use the direct parameter searching to solve the optimization problem. In this method, searching regions of

TABLE 4. Comparison of three methods.

	proposed method	standard Newton's method	direct parameter searching
Time consumption(s)	24.034602	2.264836	1505.668428
contrast	3.8866	3.3428	3.8855
entropy	9.4332	9.7683	9.4346

the three parameters center around the actual value with length 20 points, and a triple loop is executed to find the minimum of the cost function. Fig. 11h is the compensated result of this method. Because of the accurate pre-defined searching regions, image quality is relatively high. Its runtime is also shown in Table 4. As expected, the time consumption is huge, which is almost 60 times as long as that of the proposed method. And in real situations, searching regions cannot be defined accurately without prior knowledge. Therefore, this method has very low efficiency compared with the proposed method, and cannot be used directly in real cases.

Table 4 also demonstrates the contrast and entropy of imaging results obtained by the three methods. It can be concluded that our algorithm has the best performance for the highest contrast and lowest entropy.

B. REAL MEASURED DATA EXPERIMENT

In this subsection, a real measured Yak42 dataset is used to evaluate the performance of the proposed algorithm. The raw data is collected by a C-band trial radar system with $100\mu s$ pulse width and 200MHz bandwidth. The size of the echo data is 256×256 (range$\times$azimuth). Because of the intra-pulse modulation phase error, the HRRPs and image are smeared and blurred, which are demonstrated in Figs. 16a–16b. It can be seen that the HRRPs broadening effect is so obvious that the prominent scatters cannot be distinguished, and even the outline of the plane cannot be recognized.

Figs. 16c–16d illustrate the HRRPs and ISAR image obtained by the proposed method. It can be seen that through our method, the broadening effect of HRRPs is eliminated, and the image is well-focused. In Fig. 16d, detailed information like the tail of the plane and the flight attitude is clear

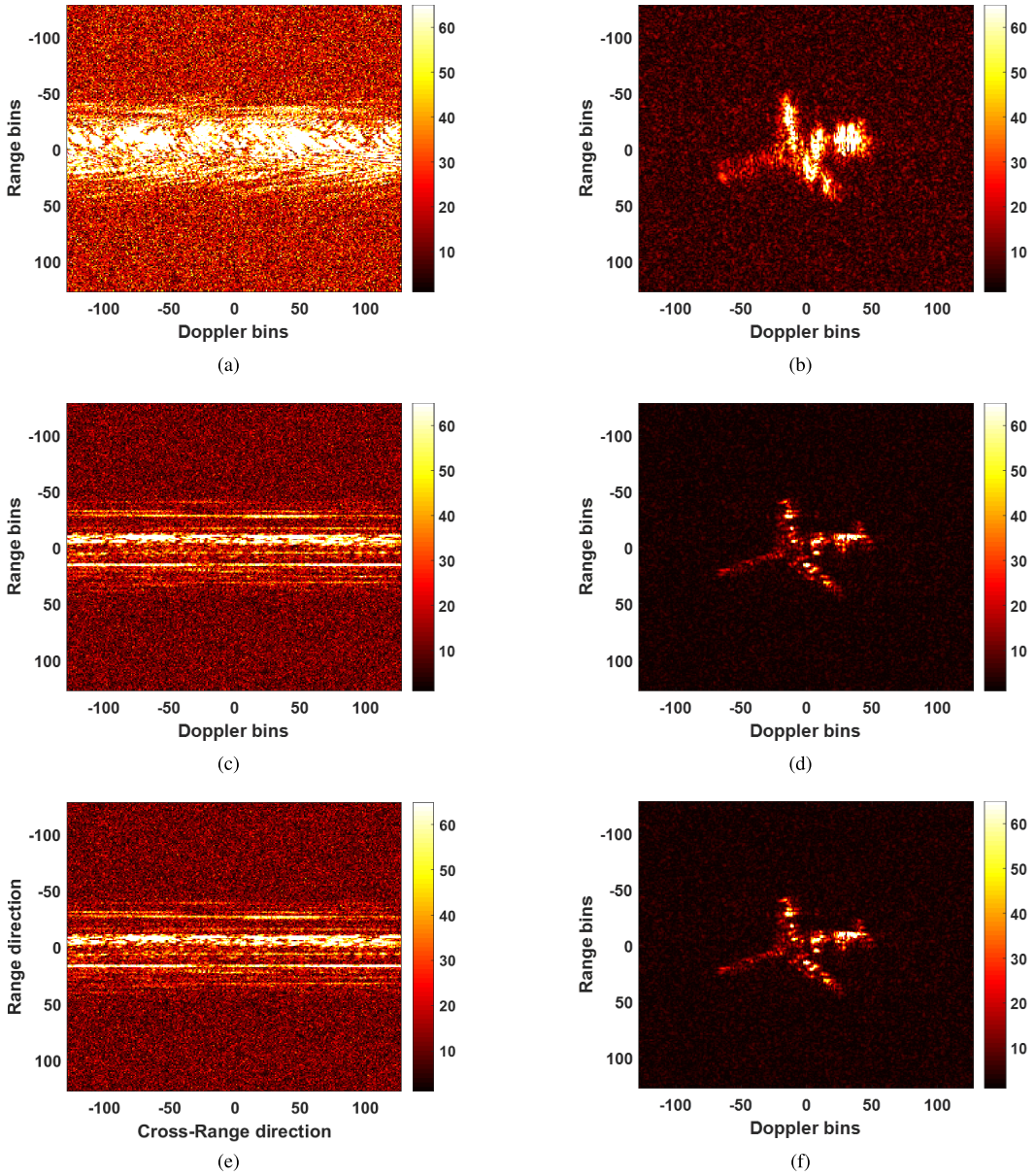

FIGURE 16. Experiment results with real measured Yak42 data. (a) The original HRRPs with phase error; (b) the imaging result without compensation; (c) the HRRPs obtained by the proposed method; (d) the imaging result obtained by the proposed method; (e) the HRRPs obtained by the standard Newton's method; (f) the imaging result obtained by the standard Newton's method.

enough. These results denote that our method is suitable for the real situation and can highly improve the imaging result. We use the contrast and entropy as the metric to evaluate the imaging quality in the same way as the simulated situation, and the evaluation results are shown in Table 5. It can be seen that the contrast increases and entropy decreases obviously compared with those of the contaminated image, which denotes a sharp and energy-focused image.

The standard Newton's method is also applied as a comparison, and its results are demonstrated in Figs. 16e–16f. It can be seen that in this situation, there is no significant difference between Figs. 16c–16d and Figs. 16e–16f through direct observation. However, the values of contrast and entropy in Table 5 denote that the quality of the image obtained by standard Newton's method is not as good as that of the image obtained by the proposed method. The contrast of Fig. 16f is lower and entropy is higher than that of Fig. 16d, which means Fig. 16d has a better degree of focus. The reason for the lower quality of the standard Newton's method is still that the standard Newton's method is apt to be trapped into local minima. Moreover, we also compare the efficiency of the two algorithms above based on the Yak42 data. The convergence curves of HRRPs' entropy produced by the two methods are shown in Fig. 17. We can see that the proposed method achieves convergence within 7 iterations (outer loops), and the CPU execution time for convergence is 0.51493 s. However, even after 50 iterations, the convergence curve of standard Newton's method still has some fluctuations (see the

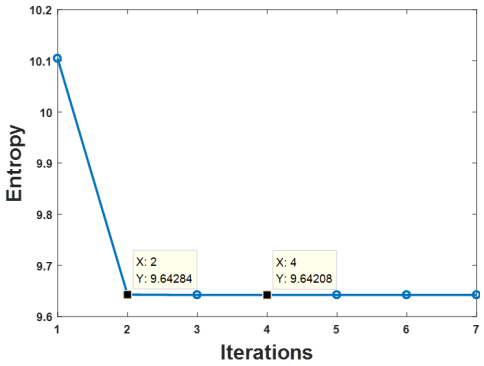

(a)

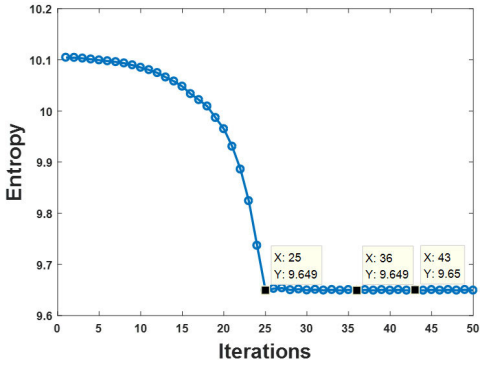

(b)

FIGURE 17. Convergence curves of the cost function. (a) the cost function's convergence curve of the proposed algorithm; (b) the cost function's convergence curve of standard Newton's method.

TABLE 5. Comparison of image quality.

	Contrast	Entropy
Contaminated image	1.1563	9.0746
Image obtained by the proposed method	1.3245	8.0904
Image obtained by the standard Newton's method	1.3228	8.1001

data cursor in Fig. 17b), and the running time for convergence is 2.54454 s. Therefore, the time consumption of the standard Newton's method is almost 5 times as long as that of the proposed method. Through the comparison, it can be proved that in real situations, the proposed algorithm has better robustness and higher efficiency than the standard Newton's method. Because of the unknown phase error parameters, the searching region of the direct parameter searching method cannot be determined accurately, therefore, we do not use direct parameter searching method as a comparison in this situation.

V. CONCLUSION

The nonlinearity of the transmitter and the nonuniformity of the target's motion can cause intra-pulse modulation phase error in received signals leading to a severely blurred ISAR image. In this paper, a 2-D time-variant phase error compensation method with accurate modeling is proposed to solve this problem. First, a novel signal model is presented to fully describe the phase error. Based on the minimum entropy principle, we secondly use the entropy of HRRPs as the cost function to estimate error parameters literately. Considering the needs for robustness and efficiency, we propose an optimization scheme combining coordinate descent algorithm with the Levenberg-Marquardt method to find the global minimum in a fast rate of convergence. Experiments have been performed with simulated and real measured data, and results indicate that the proposed method is an efficient and robust algorithm for intra-pulse modulation phase error calibration by which a well-focused ISAR image can be obtained. Furthermore, the proposed method has limitations on handling targets with low RCS in low SNR situations, which will be investigated in our furthter work.

APPENDIX

In (30), $|g(\boldsymbol{\theta})|^2$ can be expressed as

$$|g(\boldsymbol{\theta})|^2 = g(\boldsymbol{\theta}) \cdot g^*(\boldsymbol{\theta}) \tag{41}$$

Therefore, we have

$$\begin{aligned}\frac{\partial |g(\boldsymbol{\theta})|^2}{\partial \theta_k} &= \frac{\partial g(\boldsymbol{\theta}) \cdot g^*(\boldsymbol{\theta})}{\partial \theta_k} \\ &= g^*(\boldsymbol{\theta}) \cdot \frac{\partial g(\boldsymbol{\theta})}{\partial \theta_k} + g(\boldsymbol{\theta}) \cdot \frac{\partial g^*(\boldsymbol{\theta})}{\partial \theta_k}\end{aligned} \tag{42}$$

Based on the following equation

$$\frac{\partial g^*(\boldsymbol{\theta})}{\partial \theta_k} = \left[\frac{\partial g(\boldsymbol{\theta})}{\partial \theta_k}\right]^* \tag{43}$$

we can obtain

$$\begin{aligned}\frac{\partial |g(\boldsymbol{\theta})|^2}{\partial \theta_k} &= g^*(\boldsymbol{\theta}) \cdot \frac{\partial g(\boldsymbol{\theta})}{\partial \theta_k} + g(\boldsymbol{\theta}) \cdot \left[\frac{\partial g(\boldsymbol{\theta})}{\partial \theta_k}\right]^* \\ &= g^*(\boldsymbol{\theta}) \cdot \frac{\partial g(\boldsymbol{\theta})}{\partial \theta_k} + \left[g^*(\boldsymbol{\theta}) \cdot \frac{\partial g(\boldsymbol{\theta})}{\partial \theta_k}\right]^*\end{aligned} \tag{44}$$

Based on the principle that

$$a + a^* = 2Re\{a\} \tag{45}$$

where a is a complex number, (30) can be obtained with expression

$$\frac{\partial |g(\boldsymbol{\theta})|^2}{\partial \theta_k} = 2Re\left\{g^* \frac{\partial g}{\partial \theta_k}\right\} \tag{46}$$

From (30), we can get (35) directly based on (46) and the law of derivation

$$\begin{aligned}\frac{\partial^2 |g(\boldsymbol{\theta})|^2}{\partial \theta_k^2} &= 2Re\left[g(\boldsymbol{\theta})^* \frac{\partial^2 g(\boldsymbol{\theta})}{\partial \theta_k^2} + \frac{\partial g(\boldsymbol{\theta})^*}{\partial \theta_k} \frac{\partial g(\boldsymbol{\theta})}{\partial \theta_k}\right] \\ &= 2Re\left[g(\boldsymbol{\theta})^* \frac{\partial^2 g(\boldsymbol{\theta})}{\partial \theta_k^2} + \left(\frac{\partial g(\boldsymbol{\theta})}{\partial \theta_k}\right)^* \frac{\partial g(\boldsymbol{\theta})}{\partial \theta_k}\right]\end{aligned} \tag{47}$$

ACKNOWLEDGMENT

The authors would like to thank the anonymous reviewers for their enlightening comments and carefully review.

REFERENCES

[1] C.-C. Chen and H. C. Andrews, "Target-motion-induced radar imaging," *IEEE Trans. Aerosp. Electron. Syst.*, vol. AES-16, no. 1, pp. 2–14, Jan. 1980.

[2] J. L. Walker, "Range-Doppler imaging of rotating objects," *IEEE Trans. Aerosp. Electron. Syst.*, vol. AES-16, no. 1, pp. 23–52, Jan. 1980.

[3] D. A. Ausherman, A. Kozma, J. L. Walker, H. M. Jones, and E. C. Poggio, "Developments in radar imaging," *IEEE Trans. Aerosp. Electron. Syst.*, vol. AES-20, no. 4, pp. 363–400, Jul. 1984.

[4] W. Carrara, W. Carrara, R. Goodman, and R. Majewski, *Spotlight Synthetic Aperture Radar: Signal Processing Algorithms* (Artech House Remote Sensing Library). Norwood, MA, USA: Artech House, 1995.

[5] R. P. Perry, R. C. Dipietro, and R. L. Fante, "SAR imaging of moving targets," *IEEE Trans. Aerosp. Electron. Syst.*, vol. 35, no. 1, pp. 188–200, Jan. 1999.

[6] R. Vehmas, J. Jylhä, M. Väilä, J. Vihonen, and A. Visa, "Data-driven motion compensation techniques for noncooperative ISAR imaging," *IEEE Trans. Aerosp. Electron. Syst.*, vol. 54, no. 1, pp. 295–314, Feb. 2017.

[7] H. Fan, L. Ren, E. Mao, and Q. Liu, "A high-precision method of phase-derived velocity measurement and its application in motion compensation of ISAR imaging," *IEEE Trans. Geosci. Remote Sens.*, vol. 56, no. 1, pp. 60–77, Jan. 2018.

[8] H. Wu, D. Grenier, G. Y. Delisle, and D.-G. Fang, "Translational motion compensation in ISAR image processing," *IEEE Trans. Image Process.*, vol. 4, no. 11, pp. 1561–1571, Nov. 1995.

[9] M. Xing, R. Wu, and Z. Bao, "High resolution ISAR imaging of high speed moving targets," *IEE Proc.-Radar, Sonar Navigat.*, vol. 152, no. 2, pp. 58–67, 2005.

[10] Y. Gao, M. Xing, Z. Zhang, and L. Guo, "Ultrahigh range resolution ISAR processing by using KT–TCS algorithm," *IEEE Sensors J.*, vol. 18, no. 20, pp. 8311–8317, Oct. 2018.

[11] I. Cumming and F. Wong, *Digital Processing of Synthetic Aperture Radar Data: Algorithms and Implementation* (Artech House remote sensing library). Norwood, MA, USA: Artech House, 2005.

[12] P. Samczynski and K. S. Kulpa, "Coherent mapdrift technique," *IEEE Trans. Geosci. Remote Sens.*, vol. 48, no. 3, pp. 1505–1517, Mar. 2010.

[13] L. Zhang, H.-L. Li, Z.-J. Qiao, M.-D. Xing, and Z. Bao, "Integrating autofocus techniques with fast factorized back-projection for high-resolution spotlight SAR imaging," *IEEE Geosci. Remote Sens. Lett.*, vol. 10, no. 6, pp. 1394–1398, Nov. 2013.

[14] L. Zhang, M. Hu, G. Wang, and H. Wang, "Range-dependent map-drift algorithm for focusing UAV SAR imagery," *IEEE Geosci. Remote Sens. Lett.*, vol. 13, no. 8, pp. 1158–1162, Aug. 2016.

[15] G. Wang, M. Zhang, Y. Huang, L. Zhang, and F. Wang, "Robust two-dimensional spatial-variant map-drift algorithm for UAV SAR autofocusing," *Remote Sens.*, vol. 11, no. 3, p. 340, 2019.

[16] Y. Liu, Q. Hou, S. Xu, and B. Tian, "System distortion analysis and compensation of DIFS signals for wideband imaging radar," *Sci. China Inf. Sci.*, vol. 58, no. 2, pp. 1–16, 2015.

[17] J. Wang, L. Zhang, L. Du, D. Yang, and B. Chen, "Noise-robust motion compensation for aerial maneuvering target ISAR imaging by parametric minimum entropy optimization," *IEEE Trans. Geosci. Remote Sens.*, vol. 57, no. 7, pp. 4202–4217, Jul. 2019.

[18] L. Zhang, J.-L. Sheng, J. Duan, M.-D. Xing, Z.-J. Qiao, and Z. Bao, "Translational motion compensation for ISAR imaging under low SNR by minimum entropy," *EURASIP J. Adv. Signal Process.*, vol. 2013, p. 33, Dec. 2013.

[19] M. G. Czerwinski and J. M. Usoff, "Development of the haystack ultrawideband satellite imaging radar," *Lincoln Lab J.*, vol. 21, no. 1, pp. 28–44, 2014.

[20] M. Skolnik, *Introduction to Radar Systems* (Electrical Engineering Series). New York, NY, USA: McGraw-Hill, 2001.

[21] X. Li, G. Liu, and J. Ni, "Autofocusing of ISAR images based on entropy minimization," *IEEE Trans. Aerosp. Electron. Syst.*, vol. 35, no. 4, pp. 1240–1252, Oct. 1999.

[22] J. Wang and X. Liu, "Improved global range alignment for ISAR," *IEEE Trans. Aerosp. Electron. Syst.*, vol. 43, no. 3, pp. 1070–1075, Jul. 2007.

[23] D. Zhu, L. Wang, Y. Yu, Q. Tao, and Z. Zhu, "Robust ISAR range alignment via minimizing the entropy of the average range profile," *IEEE Geosci. Remote Sens. Lett.*, vol. 6, no. 2, pp. 204–208, Apr. 2009.

[24] X. Qiu, Y. Zhao, and S. Udpa, "Phase compensation for ISAR imaging combined with entropy principle," in *IEEE Antennas Propag. Soc. Int. Symp. Dig. Held Conjunct. With, USNC/CNC/URSI North Amer. Radio Sci. Meeting*, vol. 3, Jun. 2003, pp. 195–198.

[25] J. Sheng, M. Xing, L. Zhang, M. Q. Mehmood, and L. Yang, "ISAR cross-range scaling by using sharpness maximization," *IEEE Geosci. Remote Sens. Lett.*, vol. 12, no. 1, pp. 165–169, Jan. 2015.

[26] M. Martorella, F. Berizzi, and B. Haywood, "Contrast maximisation based technique for 2-D ISAR autofocusing," *IEE Proc. Radar, Sonar Navigat.*, vol. 152, no. 4, pp. 253–262, Aug. 2005.

[27] J. Nocedal and S. J. Wright, *Numerical Optimization* (Springer Series in Operations Research and Financial Engineering). New York, NY, USA: Springer, 2006.

[28] S. Ruder, "An overview of gradient descent optimization algorithms," 2016, *arXiv:1609.04747*. [Online]. Available: https://arxiv.org/abs/1609.04747

[29] N. Qian, "On the momentum term in gradient descent learning algorithms," *Neural Netw.*, vol. 12, no. 1, pp. 145–151, 1999.

[30] S. Roweis, "Levenberg-marquardt optimization," Univ. Toronto, Toronto, ON, Canada, Tech. Rep., 1996. [Online]. Available: Available: https://cs.nyu.edu/~roweis/notes/lm.pdf

[31] A. Corana, M. Marchesi, C. Martini, and S. Ridella, "Minimizing multimodal functions of continuous variables with the 'simulated annealing' algorithm Corrigenda for this article is available here," *ACM Trans. Math. Softw.*, vol. 13, no. 3, pp. 262–280, 1987.

[32] M.-W. Park and Y.-D. Kim, "A systematic procedure for setting parameters in simulated annealing algorithms," *Comput. Oper. Res.*, vol. 25, pp. 207–217, Mar. 1998.

[33] K. Deb, A. Pratap, S. Agarwal, and T. Meyarivan, "A fast and elitist multiobjective genetic algorithm: NSGA-II," *IEEE Trans. Evol. Comput.*, vol. 6, no. 2, pp. 182–197, Apr. 2002.

[34] J. Kennedy, "Particle swarm optimization," in *Encyclopedia of Machine Learning*. Boston, MA, USA: Springer, 2010, pp. 760–766.

[35] S. J. Wright, "Coordinate descent algorithms," *Math. Program.*, vol. 151, no. 1, pp. 3–34, Jun. 2015.

[36] X. Peng, Y. Wang, W. Hong, W. Tan, and Y. Wu, "Airborne downward looking sparse linear array 3-D SAR heterogeneous parallel simulation," *Remote Sens.*, vol. 5, no. 10, pp. 5304–5329, 2013.

[37] G. Franceschetti, M. Migliaccio, D. Riccio, and G. Schirinzi, "SARAS: A synthetic aperture radar (SAR) raw signal simulator," *IEEE Trans. Geosci. Remote Sens.*, vol. 30, no. 1, pp. 110–123, Jan. 1992.

[38] M. Kang, K. Ji, X. Leng, X. Xing, and H. Zhou, "Synthetic aperture radar target recognition with feature fusion based on a stacked autoencoder," *Sensors*, vol. 17, no. 1, p. 192, 2017.

[39] T. J. Kragh and A. A. Kharbouch, "Monotonic iterative algorithms for SAR image restoration," in *Proc. Int. Conf. Image Process.*, Oct. 2006, pp. 645–648.

[40] H. Erdogan and J. A. Fessler, "Monotonic algorithms for transmission tomography," *IEEE Trans. Med. Imag.*, vol. 18, no. 9, pp. 801–814, Sep. 1999.

[41] D. E. Wahl, F. H. Eichel, D. C. Ghiglia, and C. V. Jakowatz, "Phase gradient autofocus-a robust tool for high resolution SAR phase correction," *IEEE Trans. Aerosp. Electron. Syst.*, vol. 30, no. 3, pp. 827–835, Jul. 1994.

YUE LU was born in Xinjiang, China, in 1996. He received the B.S. degree in electronic and information engineering from the Beijing Institute of Technology, Beijing, China, in 2018. He is currently pursuing the M.S. degree in electronic science and technology with the Science and Technology on Automatic Target Recognition Laboratory, National University of Defense Technology, Changsha, China. His research interests include radar signal processing and inverse synthetic aperture radar imaging.

SHIYOU XU was born in Hebei, China, in 1978. He received the B.S. and Ph.D. degrees from the National University of Defense Technology, Changsha, China, in 2001 and 2008, respectively. From 2008 to 2018, he was a Lecturer with the National University of Defense Technology. He is currently an Associate Professor and a Ph.D. Supervisor with the School of Electronics and Communication Engineering, Sun Yat-sen University, Guangzhou, China. His research interests include radar signal processing and radar target recognition.

YUE ZHANG was born in Liaoning, China, in 1980. He received the Ph.D. degree in electronic science and technology from the National University of Defense Technology, Changsha, China, in 2010. His research interests include radar signal processing and automatic targets recognition.

QI WU was born in Liaoning, China, in 1995. She received the B.S. degree from the National University of Defense Technology, Changsha, China, in 2017, where she is currently pursuing the master's degree. Her current research interests include radar signal processing and automatic targets recognition.

ZENGPING CHEN was born in Fujian, China, in 1967. He received the B.S. and Ph.D. degrees from the National University of Defense Technology, Changsha, China, in 1987 and 1994, respectively, where he was a Professor and a Ph.D. Supervisor, from 1994 to 2018. He is currently a Professor and a Ph.D. Supervisor with the School of Electronics and Communication Engineering, Sun Yat-sen University. His major research interests include signal processing, radar systems, and automatic target recognition.